Redox Biology 36 (2020) 101617

Contents lists available at ScienceDirect

Redox Biology

journal homepage: www.elsevier.com/locate/redox

Research Paper

Quantitative label-free imaging of iron-bound transferrin in breast cancer cells and tumors

Ting Chean Khoo [a,1], Kate Tubbesing [b,1], Alena Rudkouskaya [b], Shilpi Rajoria [b], Anna Sharikova [a], Margarida Barroso [b,*], Alexander Khmaladze [a,**]

[a] Physics Department, SUNY University at Albany, 1400, Washington Avenue, Albany, NY, USA
[b] Department of Molecular and Cellular Physiology, Albany Medical College, 47 New Scotland Avenue, Albany, NY, 12208, USA

ARTICLE INFO

Keywords:
Transferrin
Iron metabolism
Breast cancer
Raman hyperspectral imaging

ABSTRACT

Transferrin (Tf) is an essential serum protein which delivers iron throughout the body via transferrin-receptor (TfR)-mediated uptake and iron release in early endosomes. Currently, there is no robust method to assay the population of iron-bound Tf in intact cells and tissues. Raman hyperspectral imaging detected spectral peaks that correlated with iron-bound Tf in intact cells and tumor xenografts sections (~1270-1300 cm^{-1}). Iron-bound (holo) and iron-free (apo) human Tf forms were endocytosed by MDAMB231 and T47D human breast cancer cells. The Raman iron-bound Tf peak was identified in cells treated with holo-Tf, but not in cells incubated with apo-Tf. A reduction in the Raman peak intensity between 5 and 30 min of Tf internalization was observed in T47D, but not in MDAMB231, suggesting that T47D can release iron from Tf more efficiently than MDAMB231. MDAMB231 may display a disrupted iron homeostasis due to iron release delays caused by alterations in the pH or ionic milieu of the early endosomes. In summary, we have demonstrated that Raman hyperspectral imaging can be used to identify iron-bound Tf in cell cultures and tumor xenografts and detect iron release behavior of Tf in breast cancer cells.

1. Introduction

Imbalances in iron transport resulting in dysregulation of cellular iron homeostasis are a common feature of acquired and inherited human pathologies, including neurodegenerative diseases, anemias and cancer [1–7]. Increased expression of proteins that support iron import and transport, like the transferrin receptor (TfR), has been associated with rapidly proliferating cancer cells [2,4]. What remains unclear is the regulation of transferrin (Tf)-mediated iron delivery inside the cell, and how this process could be altered during cancer progression. Furthermore, the ability to directly measure unlabeled iron-bound transport proteins while simultaneously determining their sub-cellular localization in intact cells and tissues remains a significant technical challenge.

Serum Tf is a key regulator of systemic and cellular iron transport, by binding to ferric iron (Fe^{3+}) for delivery throughout the body [8]. Iron-bound Tf binds the homodimeric TfR at the cell surface and subsequently iron-bound Tf-TfR complexes undergo clathrin-mediated endocytosis and delivery into early endosomes, where iron release occurs [8]. The structure-function of Tf-TfR complexes during iron binding and release has been thoroughly characterized using biochemical approaches, showing that both an acidic pH and specific salt concentrations are essential for the iron release from Tf-TfR complexes [8,9]. Iron-depleted Tf-TfR complexes are recycled back to the plasma membrane, where Tf dissociates from TfR into the extracellular space. Then, Tf can re-bind Fe^{3+} and undergo another transport cycle, a crucial step for maintaining systemic iron homeostasis [8]. Dysregulation of endosomal acidification or trafficking can disrupt the normal Tf cycle and therefore also iron homeostasis [10,11].

Early endocytic pathways are dysregulated in cancer cells, resulting in altered endosomal morphology, receptor signaling, recycling and degradation [12–14]. Dysregulation of endocytic acidification and salt concentration levels in cancer is associated with aggressiveness and drug resistance [15–22]. However, it is uncertain how altered endosomal trafficking impacts iron-release from Tf-TfR in cancer cells. Therefore, it is critical to develop a quantitative screening tool to measure and

* Corresponding author.
** Corresponding author.
E-mail addresses: barrosM@amc.edu (M. Barroso), akhmaladze@albany.edu (A. Khmaladze).
[1] co-first authors.

https://doi.org/10.1016/j.redox.2020.101617
Received 1 May 2020; Received in revised form 2 June 2020; Accepted 18 June 2020
Available online 24 June 2020

Abbreviations

Apo-Tf	Transferrin protein without bound iron, has ability to bind available iron at neutral pH
AF	Alexa Fluor organic dyes
EDTA	Ethylenediaminetetraacetic acid (common biological chelator)
Hepes	4-(2-hydroxyethyl)-1-piperazineethanesulfonic acid (common biological buffer)
Holo-Tf	Transferrin protein with iron in both lobes, can release iron in acidic environment
MES	2-(N-morpholino) ethanesulfonic acid (common biological buffer)
NTA	Nitrilotriacetic acid (maintains ferric iron in suspension)
Oxa-Tf	Oxalate-transferrin, a chemical mutant modified to inhibit iron release
PFA	Paraformaldehyde
PBS	Phosphate buffered saline
ROI	Region of interest
Tf	Transferrin
TfR	Transferrin receptor

visualize iron binding and release from Tf-TfR during endocytic and recycling pathway in cancer cells and tissues. Here, we use label-free techniques, such as Raman hyperspectral imaging, to measure and visualize the subcellular distribution of iron-bound proteins, which allows the correlation of their localization with morphological features of intact cells [23].

Raman microscopy is a vibrational spectroscopy technique capable of providing both qualitative and quantitative information about molecular signatures in cells and tissues. One of Raman's main advantages is that it is a noninvasive technique, which does not require chemical labels, and therefore is well-suited for biological imaging of intact cells. By combining Raman spectroscopic measurements with confocal microscopy, chemical maps of biological samples can be created, showing the localization and spatial distribution of a specific chemical in unlabeled samples [24,25]. Raman imaging techniques have been employed to provide biochemical information about proteins in unlabeled cells, tissues, and tissue engineered constructs [26–33]. In oncology, Raman spectroscopy has mainly been used to characterize and classify breast cancer cells, as well as tumor tissues [34]. These studies have provided comprehensive Raman spectral databases to discriminate breast cancer from non-cancerous tissues and evaluate tumor margins during breast cancer lumpectomy using distinct molecular signatures [35–37]. However, the usage of Raman imaging in visualization and quantification of certain protein structural properties that are associated with specific cellular processes in cancer cells and tissues is still lacking.

Here, the presence of an iron-bound Tf Raman peak in intact human breast cancer cells was validated by performing Raman hyperspectral imaging on iron-depleted human Tf (apo-Tf) and different iron-bound forms of Tf, including human native holo-Tf and "iron-locked" oxalate-Tf (oxa-Tf), which is a chemical Tf mutant that cannot efficiently release iron in acidic environment [38]. We have used Raman hyperspectral imaging to measure Tf iron-binding in estrogen receptor-positive T47D cells and triple-negative MDAMB231 human breast cancer cells [39,40]. Importantly, we have shown that iron-bound Tf displays different intracellular distribution and iron release behavior in these two distinct human breast cancer cell lines as measured by Raman imaging. Furthermore, we identified the iron-bound Tf peak in T47D and MDAMB231 tumor xenograft tissue sections. These finding have significant implications as iron transport disruption is associated with cancer metabolic heterogeneity [1–4,7,41]. In summary, these results suggest that the difference in endocytic iron release may be a critical component of the iron transport disruption in breast cancer.

2. Results

Breast cancer cells show different TfR expression, subcellular distribution and Tf uptake levels. MDAMB231 and T47D are human breast cancer model cell lines for estrogen receptor positive and triple negative breast cancer, respectively [39,40]. These cell lines were evaluated for their TfR expression and intracellular distribution, as well as Tf uptake (Fig. 1). TfR expression is regulated post-transcriptionally by the iron regulatory protein IRP1/2 based on the intracellular iron concentration [42]. Therefore, major increases in TfR expression are indicative of disrupted iron homeostasis [7]. Qualitative immunoblot analysis showed that TfR protein expression is markedly higher in T47D than in MDAMB231 cells (Fig. 1A). Nevertheless, MDAMB231 cells still displayed increased levels of TfR expression when compared to non-cancerous HMEC and HUVEC cells.

The subcellular distribution of Tf-TfR complexes is important for understanding the regulation of the endocytic trafficking pathway within cells. Changes in the size and localization of endosomes can indicate alterations in receptor regulation or endosomal acidification [11,14]. TfR endocytosis and recycling are constitutive processes, which occur continuously in the presence or absence of Tf [43]. However, Tf binding to TfR has been shown to influence endosomal trafficking rates, as well as cellular signaling [44–46]. The Tf internalization to recycling cycle varies with cell type, with the bulk of Tf recycled after 10–30 min. Interestingly, different intracellular distributions of TfR were detected in T47D and MDAMB231 cells. In MDAMB231 cells, TfR staining was localized mainly in enlarged peri-nuclear vesicular structures (Fig. 1B – top left). In contrast, T47D displayed TfR staining in small punctate structures distributed uniformly across the cell (Fig. 1B – top right). Models conveying the patterns of cell type specific TfR distribution are shown in Fig. 1B – bottom; these observations correlate with the organization of early endosome compartment in T47D and MDAMB231 cells [14]. Cells were incubated with fluorescently labeled Tf for 1 h and the cellular-associated fluorescence intensity was determined using a plate reader (Fig. 1C). Conjugation of Tf to small fluorescent dyes has been widely used to study the endocytic trafficking pathway since Tf-small dye conjugates do not significantly alter the trafficking routes of Tf [11,14,43]. Data showed that the amount of intracellular Tf is significantly higher in T47D compared to that in MDAMB231 cells following 1 h continuous incubation of AF555-Tf (Fig. 1C, Supplementary Table 1). Representative confocal images of T47D and MDAMB231 cells that were incubated with AF555-Tf for 1 h are shown in Fig. 1D. The altered intracellular distribution of Tf (Fig. 1D) is reflective of the altered TfR distributions (Fig. 1B).

Iron depleted apo-Tf and two iron-binding forms of human Tf (holo-Tf and oxa-Tf) were prepared as described in Material and Methods. To validate the preparation of chemically modified oxa-Tf and its ability to delay iron-release in an acidic environment, a spectroscopic assay was developed to measure the absorbance of Tf solutions at 470 nm over time in the presence of acidic buffer with an EDTA chelator. This assay does not directly mimic the dynamic endocytic environment, but provides a method to validate the preparation of oxa-Tf and its ability to inhibit iron release. Oxa-Tf absorbance at 470 nm is reported to decrease as iron is released from Tf in biochemistry *in vitro* assays [47]. As shown in Fig. 1E, absorbance values at 470 nm decreased significantly over time in holo-Tf in comparison to oxa-Tf (Supplementary Table 2). These results suggest that oxa-Tf releases iron at a much slower rate than holo-Tf in acidic environments.

To test these three forms of human Tf in a functional cell uptake assay, T47D and MDAMB231 cells were incubated with fluorescently labeled apo-Tf, holo-Tf, or oxa-Tf for various periods of time at 37 °C. Apo-Tf was taken up by cells significantly less than holo-Tf, as TfR has higher affinity for the latter [48]. These results showed that over time

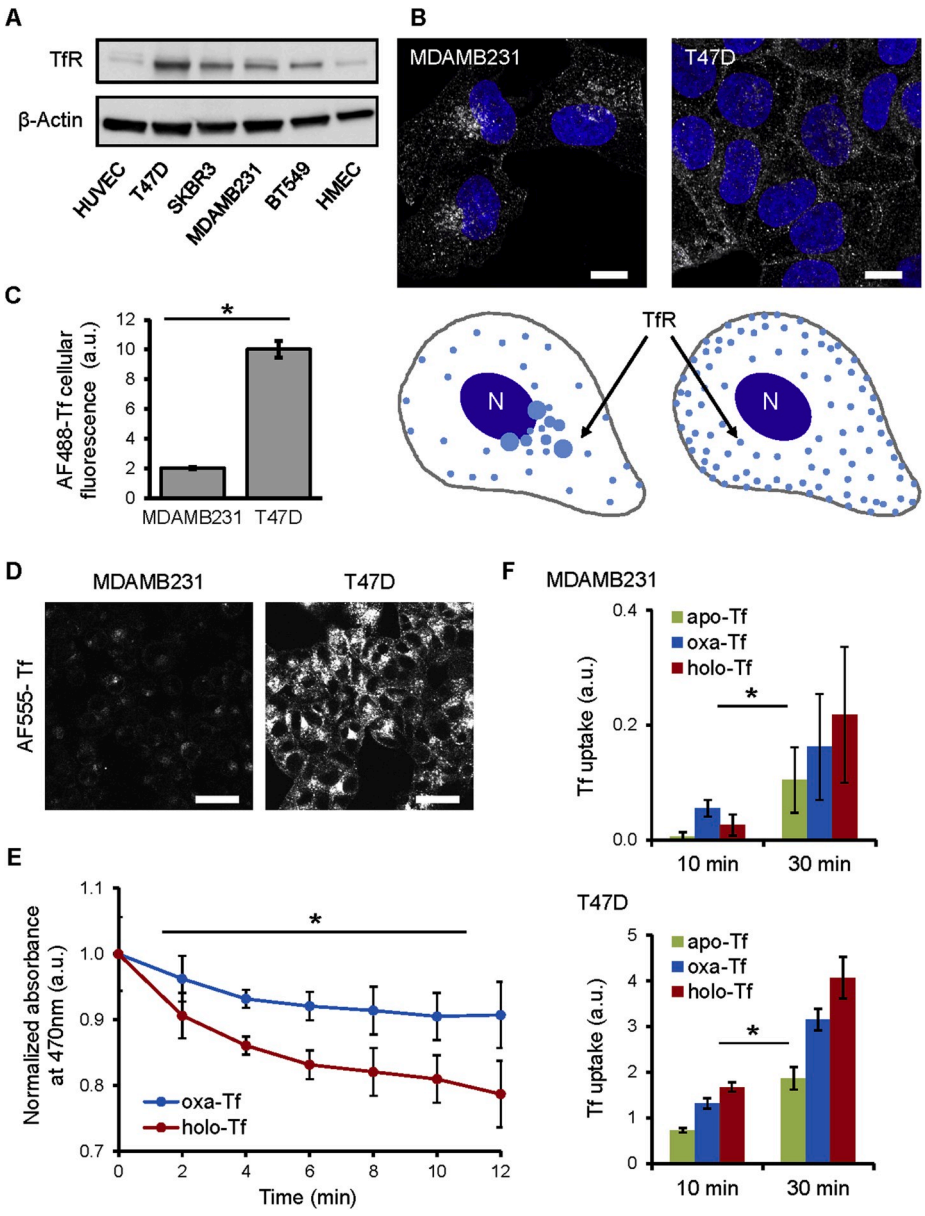

Fig. 1. TfR expression and cellular distribution and uptake of iron-binding forms of Tf in T47D vs. MDAMB231 breast cancer cells. (A) TfR expression in whole cell lysates from an endothelial cell line (HUVEC), breast cancer cell lines (T47D, SKBR3, MDAMB231, BT549 and human mammary epithelial cells (HMEC). **(B)** Fast Airy scan confocal images of cells immunostained for TfR (white) with DAPI staining of nucleus (blue); image contrast was adjusted to facilitate comparison of protein distributions between cell lines. Scale bar = 10 μm. Below each image is a model of TfR intracellular distribution for each cell line. **(C)** Cellular associated AF488-Tf measured with plate reader in MDAMB231 and T47D cells following 60 min continuous incubation. Data is presented as a mean with 95% confidence interval, n = 40 (5 reads per 8 separate wells, representative experiment). **(D)** Representative confocal images of T47D and MDAMB231 cells following 1 h incubation with AF555-Tf (50 μg/ml). Scale bar = 30 μm. **(E)** Absorbance measurements at 470 nm over-time following incubation of purified holo-Tf and oxa-Tf with acidic iron-release buffer with chelator. Data was normalized to evaluate the change in absorbance over-time and presented as a mean with 95% confidence interval, n = 4 reads from separate experiments. **(F)** Cellular associated AF555-Tf measured with plate reader in MDAMB231 and T47D cells following 10 or 30 min continuous incubation (10 μg/ml); data shown as a mean with 95% confidence interval, n = 8 per condition and time from a representative experiment. * indicates statistical significance ($p > 0.05$), Statistical summaries provided in Supplementary Tables 1–3. (For interpretation of the references to color in this figure legend, the reader is referred to the Web version of this article.)

both holo-Tf and oxa-Tf accumulated in T47D and MDAMB231 cells at similarly higher levels when compared to apo-Tf (Fig. 1F, Supplementary Table 3). In summary, these results indicate a significant difference in TfR expression and intracellular distribution, as well as in Tf uptake levels in human breast cancer cell lines. However, these results do not address the iron-bound nature of the Tf within the cells, due to the limitations of current biological assays. Label-free methods, such as Raman hyperspectral imaging, should provide further molecular information on the population of iron-bound Tf during its endocytic trafficking in breast cancer cells.

Raman spectrum peak at ~1300 cm^{-1} identifies the iron-bound state of Tf in intact cells. Firstly, we have confirmed the previously reported iron-bound Tf Raman peaks using laser excitation at 532 nm. Purified unlabeled Tf protein samples were prepared as described in Material and Methods, normalized to 2.5 mg/mL in phosphate buffered saline and their Raman spectra were acquired using 532 nm laser excitation (Fig. 2A). Raman data reveals three Raman peaks in holo-Tf, which were previously reported to be associated with iron-bound Tf molecular signature [49]: 1700 cm^{-1}, 1266-1277 cm^{-1} and 1500 cm^{-1}. Oxa-Tf has similar peaks to holo-Tf, particularly observable at the 1266-77 cm^{-1} and 1500 cm^{-1} range; subtle differences are probably due to the specific chemical modification of oxa-Tf [47]. Importantly, the apo-Tf did not share the iron-bound Tf peaks with holo-Tf and oxa-Tf (Fig. 2A). Excitation at 785 nm was similarly evaluated, but it was found to be less sensitive and specific for the detection of iron-bound Tf Raman peaks (Supplementary Fig. 1), particularly at Tf concentrations that are present in cells.

Secondly, the objective was to validate these iron-bound Tf Raman peaks, previously detected *in vitro* in purified Tf proteins (Fig. 2A), in the complex Raman spectra collected from intact, unlabeled cancer cells. The following criteria was established for the selection of the iron-bound Tf peak in cells: (i) the peak should be similar in Tf-loaded cells to that in purified Tf proteins; (ii) the peak should be higher in holo-Tf and oxa-Tf loaded cells then in apo-Tf loaded cells. T47D cells were incubated for 5 min with human purified, unlabeled apo-Tf, holo-Tf or oxa-Tf (50 μg/ml) and then subjected to Raman hyperspectral imaging. Both holo-Tf and oxa-Tf showed a stronger peak indicating an iron-bound signature at 1300 cm^{-1} upon 5 min uptake into T47D cells (Fig. 2B). Here, the iron-bound Tf peak at 1300 cm^{-1} is related to the peaks detected at 1266-1277 cm^{-1} in the purified proteins (Fig. 2A), but is slightly shifted

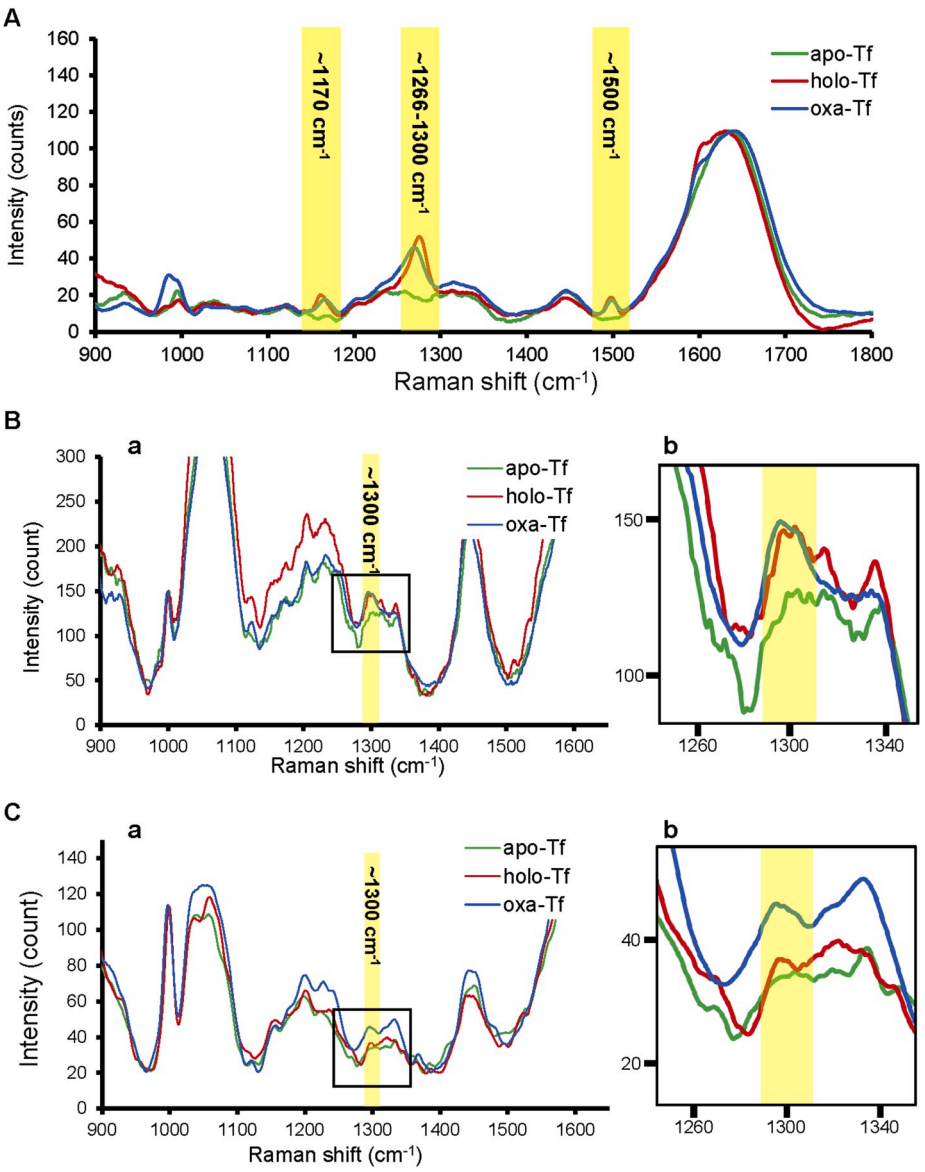

Fig. 2. Raman Peak at ~1300 cm^{-1} identifies the iron-bound state of Tf in intact breast cancer cells. (A) Raman spectra of purified apo-Tf, holo-Tf, oxa-Tf proteins in PBS buffer at 5 mg/mL on aluminum substrate at 532 nm excitation. Highlighted regions associated with iron-bound Tf. **(B–C)** Raman spectra of apo-Tf, holo-Tf and oxa-Tf (50 μg/ml) in human breast cancer T47D cells following Tf incubation for 5 min **(B)** and 60 min **(C)**, where the full spectra is to the left (**a**) and the ROI of 1300 cm^{-1} peak is enlarged on the right (**b**).

likely due to the different cellular environment and/or Tf binding to TfR at plasma membrane. Interestingly, in cells incubated with Tf for 60 min, only oxa-Tf has a significant peak at 1300 cm^{-1} (Fig. 2C), probably due the increased rate of recycling and iron-release of holo-Tf. This data indicated that 1300 cm^{-1} was a strong candidate for an iron-bound Tf peak in intact cells. Specific Raman spectra peaks detected in cells incubated with holo-Tf or oxa-Tf provide an indirect measurement of iron release, since a significant decrease in the iron-bound Tf Raman peak was predominantly detected only in cells incubated with holo-Tf. In contrast, cells incubated with oxa-Tf displayed strong iron-bound Tf Raman peak due to oxa-Tf's inhibited iron-release in acidic environment.

Visualization of peak intensities and quantification of the ~1300 cm^{-1} peak was used to monitor levels of iron-bound Tf using Raman hyperspectral imaging in intact human breast cancer cells. To account for possible contamination of the 1300 cm^{-1} Raman peak with multiple cellular components, such as saturated fatty acids and others [50,51], untreated cells were subjected to Raman microscopy under similar conditions. Raman spectra collected from these untreated cells (negative control cells) were subjected to analysis for calculation of mean intensity at 1300 cm^{-1}. A minimum of 300 Raman spectra were normally collected from untreated cells and upon data normalization to the phenylalanine peak, the mean intensity at 1300 cm^{-1} was then calculated and subtracted from 1300 cm^{-1} peak intensities acquired from cells incubated with apo-Tf, holo-Tf or oxa-Tf. This step ensures that the complex chemical composition of the cells is not contributing to quantification of ~1300 cm^{-1} iron-bound Tf peak. Fig. 3A shows typical images of scanning location and intensity per pixel for apo-Tf (panels a & d), holo-Tf (panels b & e) and oxa-Tf (panels c & f) (50 μg/ml) internalized into T47D breast cancer cells for 5 min. Based on qualitative evaluation of pixel intensity levels, both the intensity and density of pixels increased mainly in the iron-bound Tf forms (holo-Tf and oxa-Tf). ROIs indicated in Fig. 3A, panels a–c, are magnified in panels d–f, with Raman intensity levels shown in red pseudo-color range. Further quantification included the analysis of pixel density (Fig. 3B, percent of pixels with iron-bound Tf) and pixel intensity levels of iron-bound Tf peak (ROI summed and mean determined, Fig. 3C, Supplementary Table 4). The percent of pixels with iron-bound Tf provides insight into the Tf density in the ROIs and was statistically significantly higher in holo-Tf and oxa-Tf in comparison to apo-Tf (Fig. 3B). The average pixel intensity is lowest in apo-Tf and highest in oxa-Tf, while showing a significant difference between all three Tf species (Fig. 3C). Due to its

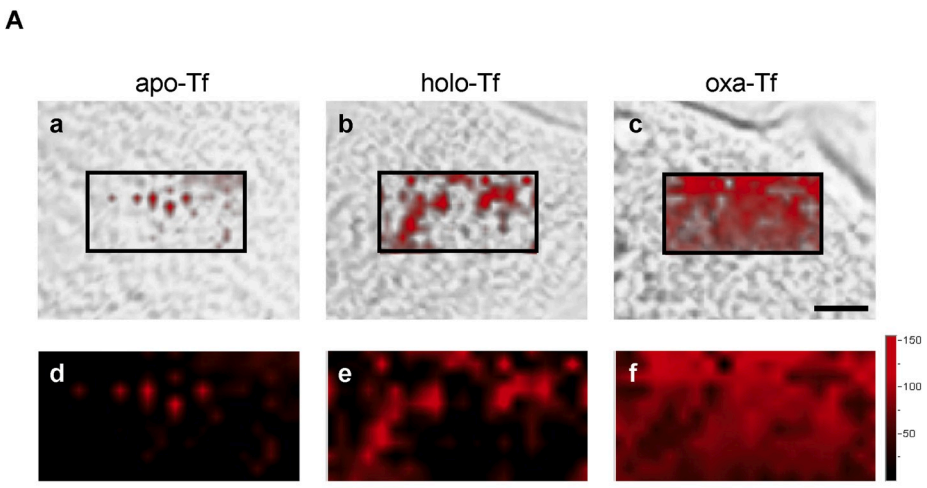

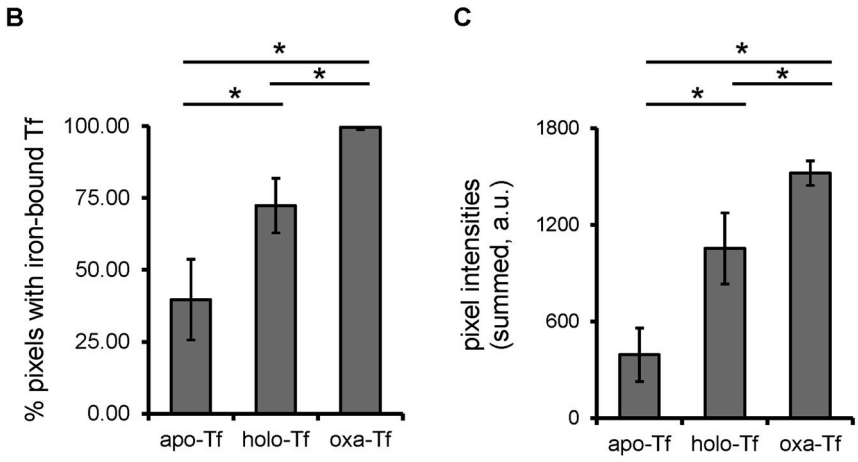

Fig. 3. Hyperspectral Raman quantitative analysis of iron-bound Tf peak in T47D cells. T47D cells incubated with apo-Tf, holo-Tf, and oxa-Tf (50 μg/mL) for 5 min were fixed and subjected to Raman hyperspectral imaging. **(A)** Representative images of T47D cells with ROI overlay displaying intensity of iron-bound Tf peak (1300 cm^{-1}) for apo-Tf (a), holo-Tf (b) and oxa-Tf (c). Additionally, the ROI is enlarged below for apo-Tf (c), holo-Tf (d) and oxa-Tf (e). There was no saturation of peak intensities; the range is modified for visualization. Scale bar = 10 μm. **(B)** Percentage of pixels per ROI with iron-bound Tf following background subtraction **(C)** the average pixel intensity (at 1300 cm^{-1}) summed per ROI following background subtraction. Representative experiment, n = 10 ROI per condition and cell line, error bars = 95% confidence interval, * indicates significance with $p > 0.05$. Statistical summary in Supplementary Table 4.

lack of iron, apo-Tf is not expected to have a significant peak intensity associated with iron-bound Tf. However, apo-Tf's ability to bind iron that may be available in the extracellular media can explain the presence of the low intensity iron-bound Raman peak upon internalization into cells (Fig. 3A and C). These results indicate that quantification of the ~1300 cm^{-1} peak intensity per pixel provides information on the nature of the iron binding capacity of Tf upon internalization into cells. Thus, Raman spectroscopy can accurately and robustly report on iron-bound Tf in intact breast cancer cells.

Iron release kinetics of Tf measured by Raman hyperspectral imaging. The iron release behavior of Tf-TfR complexes in breast cancer cells that display diverse endocytic morphology and trafficking is not well understood. Although previous studies have indicated a disrupted early endosome function in cancer cells [12–14], the iron release kinetics of Tf-TfR complexed in T47D and MDAMB231 have not been determined. Both T47D (Fig. 4A) and MDAMB231 (Fig. 4B) cells were subjected to a holo-Tf pulse-chase cell-based assay followed by Raman hyperspectral imaging. The iron-bound state of Tf was assessed after the initial 5 min pulse into cells (early endosome stage; **panels a & c**) and then after a 25 min chase period (30 min incubation total; recycling endosome step; **panels b & d**), when the bulk of Tf is expected to have its iron released into the endosomal lumen and recycled back to the surface as apo-Tf. Importantly, for each cell line, the average intensity of the 1300 cm^{-1} peak in negative control untreated cells was subtracted from all analyzed spectra to account for any cell line specific differences in composition or lipid associated peaks. Interestingly, the density and distribution of the iron-bound Tf pixels in Fig. 4A and B reflect the commonly observed TfR and Tf intracellular staining patterns (Fig. 1B and D). In particular, the perinuclear accumulation of iron-bound Tf is also clearly detected in MDAMB231 cells using Raman imaging (Fig. 4B, panel b). The quantification of the fraction of iron-bound Tf pixels showed similar density and distribution of iron-bound Tf pixels in both T47D and MDAMB231 upon 5 min Tf uptake (Fig. 4C, Supplementary Table 5). In contrast, after 30 min, the density of iron-bound Tf pixels is reduced in T47D in comparison to MDAMB231. No significant decrease was detected between 5 min and 30 min in MDAMB231 (Fig. 4C). As shown in Fig. 4D, there is a noticeable decrease in the intensity of iron-bound Tf pixels from 5 min to 30 min in T47D, but not in MDAMB231 cells. These results suggest that the population of iron-bound Tf at 30 min is larger in MDAMB231 cells, probably due to a delay in iron release (Fig. 4D, Supplementary Table 6).

In this study, the kinetics of Tf-TfR iron release in Tf pulse-chase experiments were provided by Raman hyperspectral measurements and visualization analysis. Changes in the fraction of iron-bound pixels indicate shifts in cellular distribution, whereas a reduction in intensity of iron-bound pixels suggests a loss of the iron-bound Tf population due to iron release into the endosomal lumen. A significant difference between T47D and MDAMB231 cells is detected upon 30 min Tf chase, with MDAMB231 maintaining a higher fraction and an increased intensity of iron-bound Tf pixels (Fig. 4D), suggesting significant differences in the regulation of iron release and trafficking of Tf-TfR complexes between these two breast cancer cell lines. Iron release rate was calculated by subtracting pixel intensity at 30 min from that at 5 min and then dividing it by 25 min. As shown in Supplementary Table 6, T47D had a 3.4x faster rate of iron release than MDAMB231. In summary, MDAMB231 cells do not display a decreased intensity of pixels

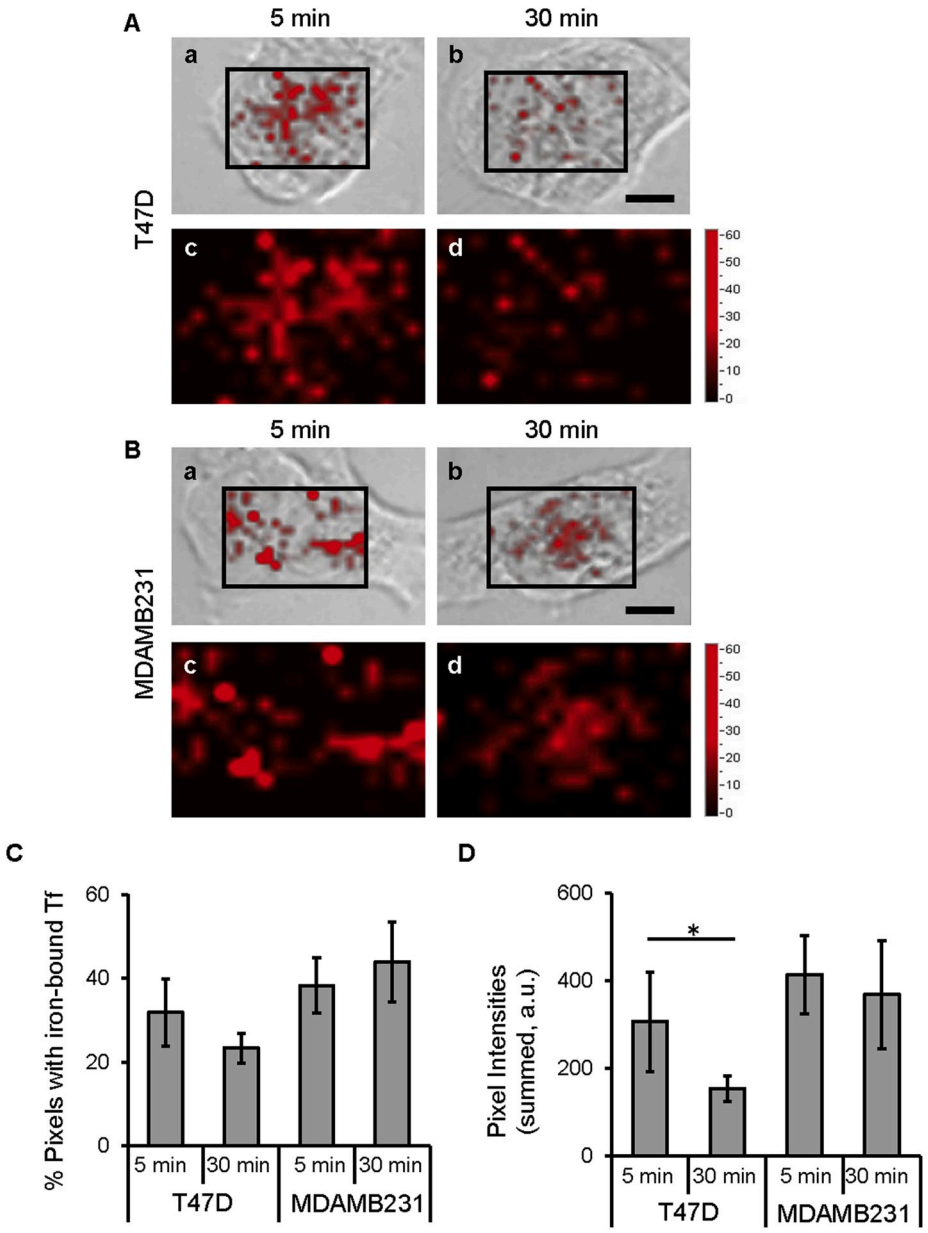

Fig. 4. Iron-release kinetics of Tf in T47D and MDAMB231 breast cancer cells. T47D and MDAMB231 cells following 5 min pulse-chase of Holo-Tf (50 μg/ml, 5 min internalization and fixation or 25 min media chase). Representative images are shown for T47D (A) and MDAMB231 (B) at 5 min (a) and 30 min (b) time points with an ROI overlay with intensity of iron-bound Tf peak (1300 cm^{-1}). Additionally, the enlarged ROI is expanded below for each time (c and d, respectively). There was no saturation of peak intensities, the range is modified for visualization. Scale bar = 10 μm. (C) percentage of pixels with iron-bound Tf following subtraction of noise threshold (D) the pixel intensity (1300 cm^{-1}) summed per ROI following subtraction of noise threshold. Representative experiment, n = 12 ROI per condition and cell line, error bars = 95% confidence interval, * indicates significance with $p > 0.05$. Statistical summary in Supplementary Tables 5–6.

associated with iron-bound Tf during the Tf-TfR endocytic pathway, suggesting that MDAMB231 may have a delay in iron release, leading to an increase in intracellular iron-bound Tf that may compensate for MDAMB231's reduced TfR expression and Tf uptake levels.

Iron-bound Tf peak measurements in breast cancer tumor xenografts. Three main reasons led us to investigate whether the iron-bound Tf peak was identifiable in tumor xenografts: (i) cell culture does not reflect complex tumor environments; (ii) TfR is overexpressed in cancer tissues, and Tf is a commonly used anti-cancer drug carrier; (iii) the release of iron from Tf is not well understood in tumor models. To determine whether the iron-bound Tf peak could be identified in tumor tissue, T47D and MDAMB231 tumor xenografts were extracted after 6h post intravenous injection of human holo-Tf and flash frozen. Raman spectra were collected from fixed T47D and MDAMD231 tumor sections at several locations randomly throughout the samples. A representative spectrum from T47D and MDAMB231 (Fig. 5A) showed that the 1300 cm^{-1} iron-bound Tf peak is distinguishable in both types of tumors. The quantification of the iron-bound Tf peak (Fig. 5B) did not show significant difference between MDAMB231 and T47D. Interestingly, the MDAMB231 cells have a wider range of peak intensity values compared to T47D (Fig. 5B), suggesting higher heterogeneity of iron-bound Tf distribution in MDAMB231 tumor sections. Immunofluorescence staining is in good agreement with Raman data, as it shows very similar density of accumulated human Tf and TfR in both types of tumors (Fig. 5C). This data indicates that following 6 h tail vein injection, there are identifiable iron-bound Tf peaks in both T47D and MDAMB231 human tumor xenografts displaying similar average intensities. Importantly, the 1300 cm^{-1} iron-bound Tf peak can be detected in both cancer cells and tumor xenografts. However, tumor environment may have significant influence on the intensity level of the 1300 cm^{-1} iron-bound Tf peak, suggesting a complex regulation of the concentration of iron-bound Tf in tumors.

3. Discussion

Recently, Raman based approaches have been used to identify specific molecular signatures associated with protein phosphorylation and tyrosine kinase inhibitors in cancer cells and tissues [52,53]. Moreover,

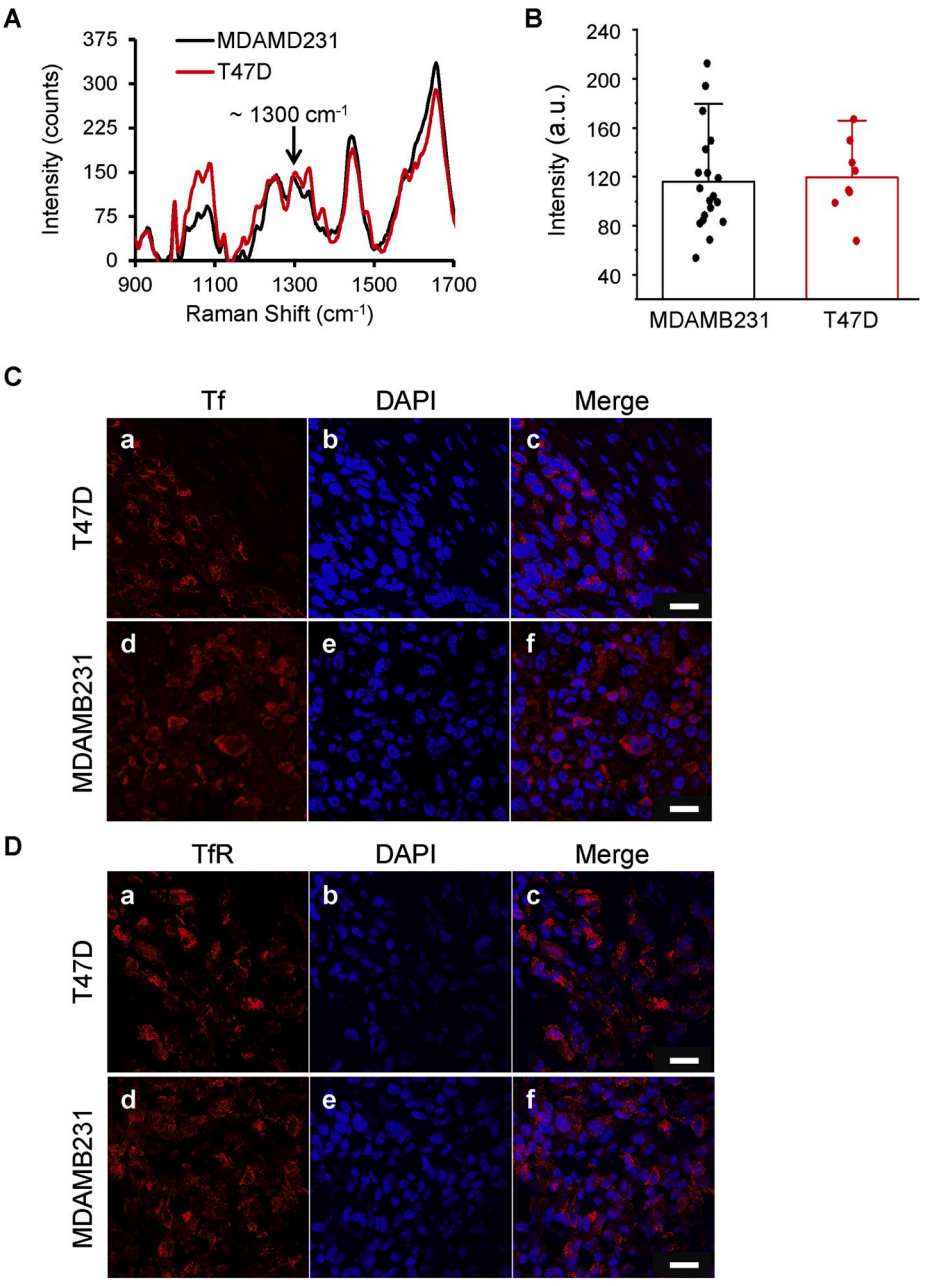

Fig. 5. Iron-bound Tf Raman signal in breast cancer tumor xenograft tissues. (A–B) Representative Raman spectra (A) and quantification of iron-bound Tf peaks (1300 cm^{-1}) (B) of human MDAMB231 and T47D breast cancer tumor xenografts collected and fixed following injection of human holo-Tf into mice. Data for (B) presented as a mean with standard deviation (bars) and raw data points overlay. Representative confocal images of MDAMB231 (Ca-c, Da-c) and T47D (Cd-f, Dd-f) tumor xenograft sections from mice injected with human holo-Tf, immunostained for anti-Tf (C, a and d) or anti-TfR (D, a & d). DAPI is shown alone (b and e) and then in a merged panel (c and f). Scale bar = 20 μm.

Raman imaging has also been used to detect lipid and glycosylation composition in breast cancer [54–57]. Here, we have used advanced Raman hyperspectral imaging to visualize and quantify the uptake and transport of unlabeled Tf with different iron-binding properties in breast cancer cells and tissues.

Standard biochemical approaches to monitoring the Tf-TfR iron release process inside acidified endosomes in cells include the measurement of total amount of iron in a cell or organelle using radioactive labeling or fluorescent iron sensors [58–60]. However, these techniques do not allow for the direct visualization and quantification of iron-bound Tf, and therefore do not provide information on Tf's ability to bind or release iron during its endocytic internalization and recycling. Here we have shown that Raman spectroscopy can provide a robust and specific method to quantify the levels of Tf-bound iron as well as to visualize the intracellular distribution of iron-bound Tf in intact, unlabeled breast cancer cells and tumor tissue sections.

While other iron measurement techniques may require labeling or destruction of the sample [61–63], Raman hyperspectral imaging allows the determination of Tf iron release kinetics in intact biological samples. The availability of apo-Tf, holo-Tf and oxa-Tf, validated for their ability to bind and release iron, permitted the identification of a specific iron-bound Tf spectral peak by Raman hyperspectral imaging in purified protein and intact cells. Most importantly, in intact cells, holo-Tf and oxa-Tf Raman peak intensity at ~1300 cm^{-1}, was significantly higher than that of apo-Tf, suggesting that it indicates iron-bound Tf specifically. The small amount of signal from apo-Tf is likely due to its ability to bind excess iron in cell media. Moreover, after 60 min internalization into cells, only oxa-Tf displayed higher levels of Raman peak intensity at ~1300 cm^{-1}, which provided a robust positive control for the Raman method since oxa-Tf, but not holo-Tf, should remain iron-bound even in acidic endosomal environments. We were also able to detect the iron-bound Tf peak in tumor tissues, indicating the utility of this method for future studies in complex tumor environments.

Using Raman hyperspectral imaging, we have mapped the

distribution of iron-bound Tf, and evaluated the number and intensity of hyperspectral pixels that contain Tf-bound iron (indicative of the cellular distribution and amount of iron-bound Tf, respectively) in T47D and MDAMB231 human breast cancer cells. The complex chemical composition of each cell line, including fatty acid profiles, may contribute to the 1300 cm^{-1} peak intensities [64]. To address this directly, negative control untreated cells were analyzed, and mean intensities at 1300 cm^{-1} subtracted from corresponding 1300 cm^{-1} Raman spectra peak collected from cells incubated with Tf. Additionally, while the ~1300 cm^{-1} Raman peak has been associated with fatty acid profiles in purified samples and lipid droplets, it is not a dominant peak utilized in fatty acid analysis of cells and tissue [51,64–66]. Importantly, hyperspectral data was superimposed over the images of analyzed cells to provide visualization of iron-bound Tf intracellular distribution. We determined that T47D cells incubated with holo-Tf for 5 min had more iron-bound Tf signal compared to cells treated with holo-Tf for 30 min, just as expected, since iron release from holo-Tf occurs early after Tf uptake upon acidification of endosomal pathway [60]. In contrast, the iron-bound Tf pixel intensity and distribution were maintained at similar levels from 5 min to 30 min of Tf pulse-chase in MDAMB231 cells. Label-free measurement of iron-bound Tf inside cells using Raman imaging can reveal alterations in iron release in early endosomal populations. Increased iron-bound Tf over time indicates potential disruption of early endosomal regulation including, but not limited to, endosomal acidification. Furthermore, iron-bound Tf containing pixels in MDAMB231 cells are distributed in a peri-nuclear pattern that is similar to TfR immunofluorescence staining. These results indicate that MDAMB231's altered endosomal morphology correlates with altered iron-binding and release dynamics that appears delayed in comparison to that of T47D cells.

Breast cancer cells can differ significantly in the expression and cellular distribution of TfR as well as in the level of Tf uptake [14,41]. However, these results do not provide further information on the iron-bound nature of Tf uptake and localization. Interestingly, our results show an apparent contradiction, in which MDAMB231 cells accumulate less Tf compared to T47D, but then display a higher percent of

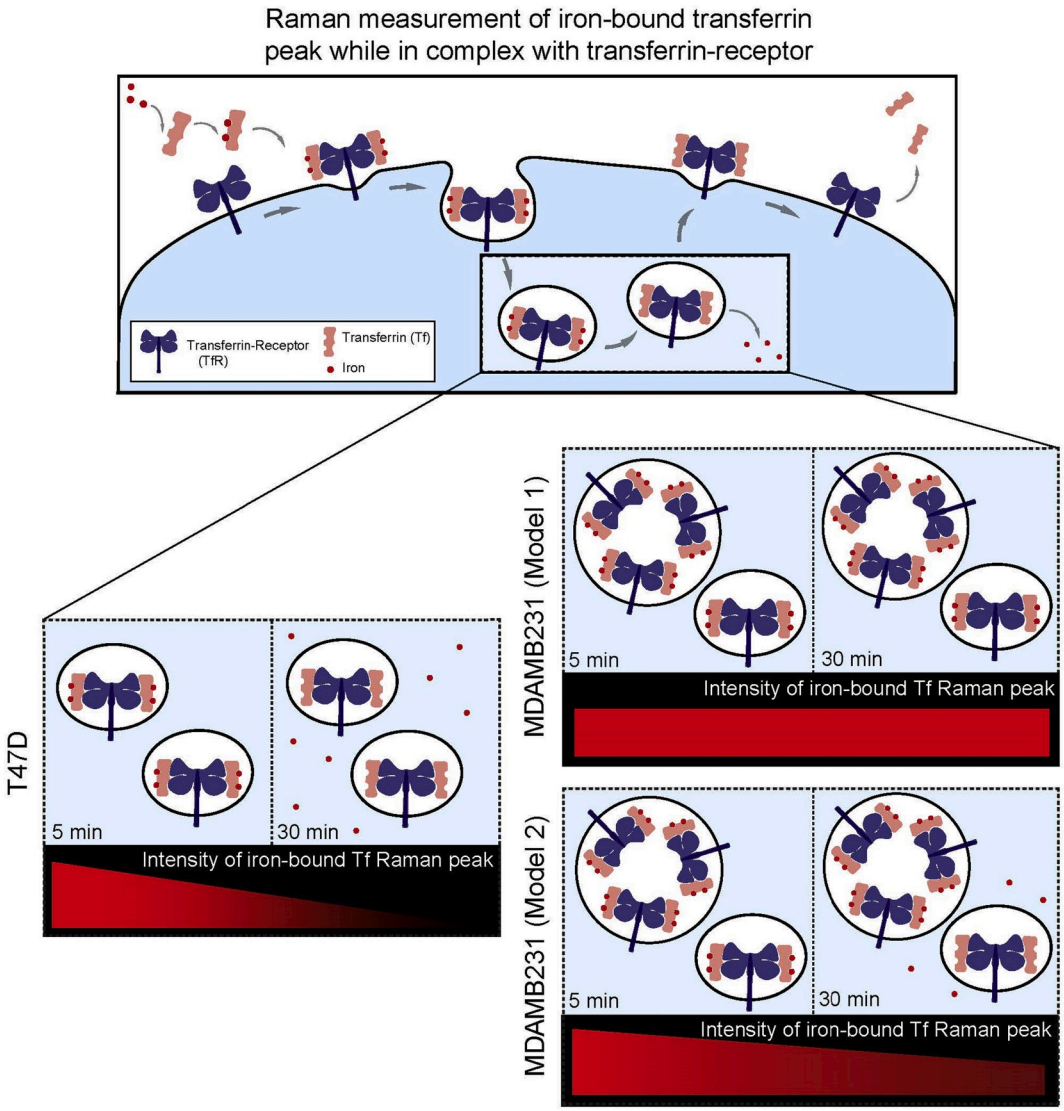

Fig. 6. Model - Raman measurement of iron-bound Tf peak while in complex with TfR in two distinct breast cancer cell lines. Tf binds TfR at cell surface forming a Tf-TfR complex. The complex undergoes endocytosis, iron is released in mildly acidic endosome and Tf-TfR complex recycles back to the cell surface where Tf is released. T47D and MDAMB231 differ in endocytic organization and function [14], they also differ in the intensity of iron-bound Tf over time. T47D has a significant decrease in the intensity of iron-bound over time which is associated with normal iron-release from Tf. MDAMB231 does not have a significant decrease in iron-bound Tf over-time which may be due from abnormal acidification or trafficking which inhibits iron-release in all compartments (Model 1) or from distinctly altered compartments (Model 2).

iron-bound Tf-TfR complexes upon Tf uptake. Thus, the data suggests that T47D may release iron from Tf more efficiently than MDAMB231 (Fig. 6). We propose that a slower rate of iron release in MDAMB231 in comparison to that of T47D is at the basis of these results, compensating for MDAMB231's reduced TfR expression and Tf uptake levels. MDAMB231 cells could display a disrupted iron homeostasis due to iron release delays caused by alterations in the pH or ionic milieu of the early endosomes. Delays in iron release from Tf into the endosomal lumen may subsequently affect delivery of iron into mitochondria or cytosol. Integrating TfR expression and Tf uptake measurements with Raman hyperspectral imaging of iron-bound Tf provides a comprehensive understanding of iron homeostasis and endosomal function in breast cancer cells.

In summary, Raman hyperspectral imaging at ~1300 cm^{-1} can be used to identify iron-bound Tf in cell culture and tumor xenografts. Immunofluorescence staining is in good agreement with Raman data, as it shows very similar density of accumulated human Tf and TfR in both types of tumors. While the 1300 cm^{-1} iron-bound Tf peak can be detected in both cancer cells and tumor xenografts, tumor environment may have significant influence on the intensity level of this peak, which suggests a complex regulation of the concentration of iron-bound Tf in tumors. Further investigation of iron release kinetics and pixel distributions are required to understand iron-release in tumor tissues.

4. Conclusion

We have demonstrated that Raman hyperspectral imaging can be used to identify iron-bound Tf in unlabeled intact breast cancer cells and tumor xenografts, which represents a novel approach to understanding intracellular iron regulation in intact biological samples. Our data identified important differences in iron-release kinetics between breast cancer cell lines, and the Raman hyperspectral imaging was reflective of associated endosomal morphologies. Our data also indicates heterogeneity in the regulation of iron uptake and release in human breast cancer cells. Further development of Raman hyperspectral imaging technology and additional correlative microscopy techniques will be essential to enhance our understanding of iron regulation in breast cancer.

5. Material and methods

Transferrin preparation and validation. Human Tf (Sigma, cat #T1147) was reconstituted in phosphate buffered saline solution (PBS, pH 7.4) at 10 mg/mL and subjected to either (1) iron removal to produce apo-Tf, (2) iron loading to generate holo-Tf or (3) iron loading with oxalate to produce oxa-Tf. Buffer exchanges and washing steps were performed with Amicon Ultra 30K micro concentrators (Millipore UFC803024). Protocol for iron removal consisted of incubating Tf in 0.5 M sodium acetate, pH 4.9, containing 1 mM Nitrilotriacetic acid (NTA, Sigma NO128) and 1 mM Ethylenediaminetetraacetic acid (EDTA, Fisher-Scientific S80007-1) for 1 h at room temperature. Then Tf was washed first with 0.1 M sodium perchlorate in PBS, followed by washing with 0.1 M KCl in PBS. Apo-Tf was maintained in PBS at 1 mg/ml. Iron loading requires exchanging Tf into a 50 mM 4-(2-hydroxyethyl)-1-piperazineethanesulfonic acid (Hepes, Sigma H4034) and 20 mM sodium bicarbonate buffer (Sigma S7277). Iron-loading stock solutions included a 25 mM ferrous ammonium sulfate (Sigma 215406) in 0.01 N HCl and 100 mM NTA in purified water. Tf was incubated with a freshly prepared Fe(III)-NTA solution in a 1:2 M ratio, protected from light and under gently rocking motion at room temperature for 1–2 h. Iron loading for oxa-Tf was similar, with the main difference being an initial exchange of Tf into a 200 mM Potassium oxalate (Honeywell-Fluka 60425) in purified water. Excess Fe (III)-NTA was removed by performing several wash steps using micro concentrators. Tf preparations were diluted to 1 mg/mL in PBS and stored at −20 °C until the day of experiment.

A spectroscopic assay was developed to measure the absorbance of Tf solutions at 470 nm over time in the presence of acidic buffer. The absorbance at 470 nm is reported to decrease as iron is released from Tf [47]. Equal volumes of 50 mM MES, 4 mM EDTA, pH 5.6 and Tf solutions (oxa-Tf or holo-Tf at 1 mg/mL in PBS) were added to UV-clear plastic 96-well (half-area) plate, and absorbance at 470 nm was measured every minute for 30 min at 25 °C using a Flexstation III (Molecular Devices). Each experiment was normalized to the earliest time point collected (0 min), to allow for the comparison of absorbance measurements over time. Experiments were averaged and subjected to statistical analysis (two-factor anova). A portion of prepared Tf was subjected to Alexa Fluor 488 or 555 fluorescent labeling (ThermoFisher, A20009 or A20000) according to manufacturer's protocols.

Cell culture. T47D, MDAMB231 and SKBR3 human breast cancer cell lines were purchased from ATCC and tested routinely for mycoplasma by both PCR and high resolution DAPI imaging methods. T47D and MDAMB231 cells were cultured in DMEM (Gibco 11965–092) with 10% fetal bovine serum (FBS, ATCC 30–2020), 4 mM L-glutamine and 10 mM HEPES. SKBR3 cells were cultured in McCoy's 5A medium (ATCC 30–2007) with 10% FBS and 10 units penicillin/500 ml media, 10 μg streptomycin/500 ml media. HMEC and HUVEC were purchased from Lonza and cultured according to manufacturer's instruction. Clear imaging media consisted of phenol red-free DMEM with 0.5% Bovine Serum albumin, 4 mM L-glutamine and 20 mM HEPES. HMEC cells were cultured in MEGM media (Lonza CC-3051A) with MEGM singleQuots (Lonza CC-4136).

Western blotting. Whole cell lysates were prepared with a 2% SDS, 8 mM EDTA lysis buffer (SDS Sigma L4390, EDTA Fisher S80007-1). Lysates were normalized to equal protein levels determined using Thermo Scientific NanoDrop Lite, then denatured with heat (95 °C) in 5x Laemmli buffer. Lysates were run on 4–20% gels (Biorad 456-1094) with Tris/Glycine/SDS (Biorad 161-0732), followed by transfer to nitrocellulose paper with standard 20% methanol transfer buffer. Membranes were blocked with 5% dried milk in TBST, followed by primary antibody incubation for 2 h at room temperature. Membranes were then washed and subjected to incubation with secondary horseradish peroxidase-conjugated antibodies (Cell signaling). Proteins were visualized using enhanced chemiluminescence (ECL) reagents (Biorad) and captured using Amersham Imager 600 (GE Healthcare).

Tf uptake plate-reader assay. Cells were grown to near confluence (24–36 h) in a heated incubator, washed and subjected to 30 min pre-incubation with clear imaging media. All steps prior to fixation were at 37 °C. Cells were then incubated with AF647-Tf (10 μg/ml) in clear media for 1 h, then fixed with 4% paraformaldehyde (PFA) for 15 min at room temperature. Since each cell line contributes a unique background signal on the plate reader, cells without fluorescent labeling were incorporated into each plate for background subtraction. Measurement of total cellular fluorescence was performed using a Flexstation III (Molecular Devices) with associated SoftmaxPro5 software (bottom-read, 5-reads per well).

Tumor xenografts. All animal procedures were conducted with the approval of the Institutional Animal Care and Use Committee at Albany Medical College. Animal facility has been accredited by the American Association for Accreditation for Laboratory Animals Care International. Tumor xenografts were generated by injecting 10×10^6 T47D cells or 1×10^6 MDAMB231 in PBS mixed 1:1 with Cultrex BME (R&D Systems Inc, Minneapolis, MN, USA) into the right inguinal mammary fat pad of female 4-week old athymic nude mice (NU(NCr)-Foxn1nu, Charles River Laboratories, Wilmington, MA, USA). The subcutaneous tumors were allowed to grow for 4–5 weeks and were monitored daily. The animals were intravenously injected with human holo-Tf (40 μg in the volume 100 μl) and sacrificed 6 h post injection. The excised tumors were either flash frozen for immunofluorescent analysis.

Immunofluorescent microscopy. For fluorescently-labeled AF555-Tf uptake, cells were pre-incubated with clear imaging media for 30 min prior to 1h internalization of AF555-holo-Tf. For both Tf uptake and immunofluorescence (IF), cells were fixed for 15 min with 4% PFA at

room temperature. For IF, cells were permeabilized with 0.1% TX-100 in PBS (ThermoFisher BP151) for 15 min at room temperature, blocked for 90 min on a gentle rocker-shaker in 2% fish skin gelatin (FGS, Millipore-Sigma, catalog #G7765), 1% BSA in PBS. Subsequent washing and antibody blocking were performed using 0.5% FSG, 0.05% TX-100 in PBS. All solutions were 0.2 μm syringe filtered. Frozen sections of tumor xenografts (10 μm) were fixed with 2% PFA, permeabilized with 0.3% Triton X-100 and processed for immunostaining following MOM protocol (Vector labs). Antibodies used: anti-mouse TfR (Abcam 38171) 1:200, anti-mouse Tf (Serotech 9100–1057) 1:200, Fab goat anti-mouse AF555, 1:250 (Invitrogen). The images were acquired using Zeiss 510 LSM microscope or Zeiss 880 LSM with Fast Airyscan detector.

Raman spectroscopy. Raman spectra were acquired by XploRA PLUS Raman microscope (HORIBA). The system was equipped with a 1024 × 256 TE air cooled CCD chip (pixel size 26-μm, temperature −60 °C). HORIBA LabSpec6 software was used for data acquisition, normalization, fluorescent background removal, and baseline correction. Entrance slit was set to 50 μm, which yielded a spectral resolution of 4 cm^{-1}.

Raman imaging of Tf. The spectra of apo-Tf, holo-Tf and oxa-Tf protein droplets were collected with a 10x objective, 532 nm excitation laser wavelength at 100% power, 1800 gr/mm grating. The droplets were deposited on aluminum foil, and the spectra were taken from several locations within each droplet. The spectra were background subtracted, averaged and normalized.

Raman imaging of cells or tumor xenografts following Tf internalization. Cells were grown on quartz substrates coated with poly-D-lysine. Cells were pre-incubated with clear imaging media for 30 min prior to Tf internalization (time and concentration specified in Figure legends). Following Tf internalization, cells were fixed with ice-cold 4% PFA and immersed in PBS buffer solution (pH 7.0). Control cells, specific to each cell line evaluated, were not incubated with Tf but were otherwise prepared, fixed and analyzed in an identical manner. Frozen tumor xenografts were sectioned at 10 μm, transferred to quartz substrates, fixed in 4% PFA and imaged in PBS buffer.

The spectra of cells and tissues were taken with 20x Olympus immersion objective, 532 nm excitation laser at 100% power, and 1800 gr/mm grating. Total 220–300 spectra/sample were collected for large region of interest (ROI) in cell samples. In hyperspectral cell imaging, 1300 cm^{-1} Raman Tf peak was used for mapping, the mean intensity of control cells was subtracted from each spectra analyzed. Raman spectra of tissue samples were taken from several locations within the tissue. At least three different locations were used in collection of large ROIs, which were separated into smaller regions. Pixels that did not directly overlap with the cell area were removed from analysis.

Statistical Analysis. Statistical analysis included two-tailed student t-tests or two-factor anova analysis. Post-hoc testing included Bonferroni correction as required with multiple comparisons.

Author contributions

Initial idea and concepts developed by A.K. and M.B., which evolved to current form with input from all authors. K.T. contributed Tf preparations and validation studies. S.R. and K.T contributed to cell culture, western blot, Tf uptake studies and confocal imaging. A.R. contributed to all tumor xenograft associated data. T.K. contributed Raman imaging for cells and tissues, processing and visualization. T.K. and A.S. contributed to Raman imaging of Tf protein. T.K. and K.T contributed to Raman analysis and statistical analysis. T.K, K.T., A.S., M.B., and A.K. contributed to writing and editing of manuscript.

Declaration of competing interest

The authors declare no competing interests.

Acknowledgements

The authors would like to thank Dr. Anne Mason for discussions on iron release in cancer cells. We thank the AMC imaging core facility for the use of the Zeiss LSM880 and LSM510 confocal microscopes. We thank all members of the Barroso and Khmaladze laboratories for their stimulating discussion. We would like to acknowledge and thank Lauren Elder for her help with the model design in Fig. 6. This work was supported by the National Institutes of Health RO1 CA207725 and RO1 CA233188 to Dr. Barroso and RO1 DA047410-01 grant to Dr. Khmaladze.

Appendix A. Supplementary data

Supplementary data to this article can be found online at https://doi.org/10.1016/j.redox.2020.101617.

References

[1] L.M. Bystrom, S. Rivella, Cancer cells with irons in the fire, Free Radic. Biol. Med. 79 (2015) 337–342.
[2] D.H. Manz, N.L. Blanchette, B.T. Paul, F.M. Torti, S.V. Torti, Iron and cancer: recent insights, Ann. N. Y. Acad. Sci. 1368 (2016) 149–161.
[3] P.-J. Lamy, A. Durigova, W. Jacot, Iron homeostasis and anemia markers in early breast cancer, Clin. Chim. Acta 434 (2014) 34–40.
[4] S.V. Torti, F.M. Torti, Iron and cancer: more ore to be mined, Nat. Rev. Canc. 13 (2013) 342–355.
[5] R.E. Fleming, P. Ponka, Iron overload in human disease, N. Engl. J. Med. 366 (2012) 348–359.
[6] T. Ganz, E. Nemeth, Hepcidin and disorders of iron metabolism, Annu. Rev. Med. 62 (2011) 347–360.
[7] H. Ye, T.a. Rouault, Human iron-sulfur cluster assembly, cellular iron homeostasis, and disease, Biochemistry 49 (2010) 4945–4956.
[8] A.N. Luck, A.B. Mason, Transferrin-mediated cellular iron delivery, in: Current Topics in Membranes, 69, 2012, pp. 3–35.
[9] S.L. Byrne, N.D. Chasteen, A.N. Steere, A.B. Mason, The unique kinetics of iron release from transferrin: the role of receptor, lobe–lobe interactions, and salt at endosomal pH, J. Mol. Biol. 396 (2010) 130–140.
[10] G. Baravalle, et al., Transferrin recycling and dextran transport to lysosomes is differentially affected by bafilomycin, nocodazole, and low temperature, Cell Tissue Res. 320 (2005) 99–113.
[11] K.M. Mayle, A.M. Le, D.T. Kamei, The intracellular trafficking pathway of transferrin, Biochim. Biophys. Acta 1820 (2012) 264–281.
[12] I. Mellman, Y. Yarden, Endocytosis and cancer, Cold Spring Harb. Perspect. Biol. 5 (2013) a016949–a016949.
[13] S.L. Schmid, Reciprocal regulation of signaling and endocytosis: implications for the evolving cancer cell, J. Cell Biol. 216 (2017) 2623–2632.
[14] K. Tubbesing, et al., Complex Rab4-mediated regulation of endosomal size and EGFR activation, *Mol. Cancer Res.* molcanres. (2020), https://doi.org/10.1158/1541-7786.MCR-19-0052, 0052.2019.
[15] S. Pamarthy, et al., The Vacuolar ATPase a2-subunit regulates Notch signaling in triple-negative breast cancer cells, Oncotarget 6 (2015) 34206–34220.
[16] Q. Lu, et al., The expression of V-ATPase is associated with drug resistance and pathology of non-small-cell lung cancer, Diagn. Pathol. 8 (2013) 145.
[17] J. Capecci, M. Forgac, The function of vacuolar ATPase (V-ATPase) a subunit isoforms in invasiveness of MCF10a and MCF10CA1a human breast cancer cells, J. Biol. Chem. 288 (2013) 32731–32741.
[18] A. Hinton, et al., Function of a subunit isoforms of the V-ATPase in pH homeostasis and in vitro invasion of MDA-MB231 human breast cancer cells, J. Biol. Chem. 284 (2009) 16400–16408.
[19] C.C. Scott, J. Gruenberg, Ion flux and the function of endosomes and lysosomes: pH is just the start, Bioessays 33 (2011) 103–110.
[20] T.J. Jentsch, Chloride and the endosomal-lysosomal pathway: emerging roles of CLC chloride transporters, J. Physiol. 578 (2007) 633–640.
[21] F. Lucien, et al., Hypoxia-induced mobilization of NHE6 to the plasma membrane triggers endosome hyperacidification and chemoresistance, Nat. Commun. 8 (2017) 15884.
[22] M. Peretti, et al., Chloride channels in cancer: focus on chloride intracellular channel 1 and 4 (CLIC1 AND CLIC4) proteins in tumor development and as novel therapeutic targets, Biochim. Biophys. Acta Biomembr. 1848 (2015) 2523–2531.
[23] C. Yu, E. Gestl, K. Eckert, D. Allara, J. Irudayaraj, Characterization of human breast epithelial cells by confocal Raman microspectroscopy, Canc. Detect. Prev. 30 (2006) 515–522.
[24] L. Sfakis, et al., Core/shell nanofiber characterization by Raman scanning microscopy, Biomed. Optic Express 8 (2017) 1025.
[25] A. Sharikova, et al., Characterization of nanofibers for tissue engineering: chemical mapping by Confocal Raman microscopy, Spectrochim. Acta Part A Mol. Biomol. Spectrosc. 227 (2020) 117670.
[26] J. Jasensky, et al., Live-cell quantification and comparison of mammalian oocyte cytosolic lipid content between species, during development, and in relation to

body composition using nonlinear vibrational microscopy, Analyst (2016), https://doi.org/10.1039/c6an00629a.
[27] A. Khmaladze, et al., Tissue-engineered constructs of human oral mucosa examined by Raman spectroscopy, Tissue Eng. C Methods 19 (2013) 299–306.
[28] J.D.P. McElderry, et al., Tracking circadian rhythms of bone mineral deposition in murine calvarial organ cultures, J. Bone Miner. Res. (2013), https://doi.org/10.1002/jbmr.1924.
[29] A. Khmaladze, et al., Hyperspectral imaging and characterization of live cells by broadband coherent anti-Stokes Raman scattering (CARS) microscopy with singular value decomposition (SVD) analysis, Appl. Spectrosc. (2014), https://doi.org/10.1366/13-07183.
[30] P.I. Okagbare, M.D. Morris, Polymer-capped fiber-optic Raman probe for non-invasive Raman spectroscopy, Analyst 137 (2012) 77–81.
[31] J.-D.P. McElderry, M.R. Kole, M.D. Morris, Repeated freeze-thawing of bone tissue affects Raman bone quality measurements, J. Biomed. Optic. 16 (2011), 071407.
[32] K.A. Dooley, J. McCormack, D.P. Fyhrie, M.D. Morris, Stress mapping of undamaged, strained, and failed regions of bone using Raman spectroscopy, J. Biomed. Optic. 14 (2009), 044018.
[33] W.-L. Lo, et al., Raman spectroscopy monitoring of the cellular activities of a tissue-engineered ex vivo produced oral mucosal equivalent, J. Raman Spectrosc. 42 (2011) 174–178.
[34] G.W. Auner, et al., Applications of Raman spectroscopy in cancer diagnosis, Canc. Metastasis Rev. 37 (2018) 691–717.
[35] F.M. Lyng, et al., Discrimination of breast cancer from benign tumours using Raman spectroscopy, PloS One 14 (2019) 1–13.
[36] W. Zuniga, et al., Raman spectroscopy for rapid evaluation of surgical margins during breast cancer lumpectomy, Sci. Rep. 9 (2019) 14639.
[37] R. Galli, et al., Identification of distinctive features in human intracranial tumors by label-free nonlinear multimodal microscopy, J. Biophot. 12 (2019), e201800465.
[38] P.J. Halbrooks, A.B. Mason, T.E. Adams, S.K. Briggs, S.J. Everse, The oxalate effect on release of iron from human serum transferrin explained, J. Mol. Biol. 339 (2004) 217–226.
[39] S.E. Smith, et al., Molecular characterization of breast cancer cell lines through multiple omic approaches, Breast Cancer Res. (2017), https://doi.org/10.1186/s13058-017-0855-0.
[40] R.M. Neve, et al., A collection of breast cancer cell lines for the study of functionally distinct cancer subtypes, Canc. Cell 10 (2006) 515–527.
[41] A. Rudkouskaya, et al., Quantitative imaging of receptor-ligand engagement in intact live animals, J. Contr. Release 286 (2018) 451–459.
[42] C.P. Anderson, M. Shen, R.S. Eisenstein, E.a. Leibold, Mammalian iron metabolism and its control by iron regulatory proteins, Biochim. Biophys. Acta Mol. Cell Res. 1823 (2012) 1468–1483.
[43] F.R. Maxfield, T.E. McGraw, Endocytic recycling, Nat. Rev. Mol. Cell Biol. 5 (2004) 121–132.
[44] N. Gironès, R.J. Davis, Comparison of the kinetics of cycling of the transferrin receptor in the presence or absence of bound diferric transferrin, Biochem. J. 264 (1989) 35–46.
[45] V. Yashunsky, et al., Real-time monitoring of transferrin-induced endocytic vesicle formation by mid-infrared surface plasmon resonance, Biophys. J. 97 (2009) 1003–1012.
[46] H. Cao, J. Chen, E.W. Krueger, M.A. McNiven, SRC-mediated phosphorylation of dynamin and cortactin regulates the 'constitutive' endocytosis of transferrin, Mol. Cell Biol. 30 (2010) 781–792.
[47] M.G. Patch, C.J. Carrano, The origin of the visible absorption in metal transferrins, Inorg. Chim. Acta. 56 (1981) L71–L73.
[48] B.E. Eckenroth, A.N. Steere, N.D. Chasteen, S.J. Everse, A.B. Mason, How the binding of human transferrin primes the transferrin receptor potentiating iron release at endosomal pH, Proc. Natl. Acad. Sci. Unit. States Am. 108 (2011) 13089–13094.
[49] C. Frank, O. Rienitz, R. Jährling, D. Schiel, S. Zakel, Reference measurement procedures for the iron saturation in human transferrin based on IDMS and Raman scattering, Metall 4 (2012) 1239.
[50] E. Matuszyk, et al., Differential response of liver sinusoidal endothelial cells and hepatocytes to oleic and palmitic acid revealed by Raman and CARS imaging, Biochim. Biophys. Acta (BBA) - Mol. Basis Dis. 1866 (2020) 165804.
[51] S. You, et al., Raman spectroscopic analysis reveals abnormal fatty acid composition in tumor micro- and macroenvironments in human breast and rat mammary cancer, Sci. Rep. 6 (2016) 1–10.
[52] H. Abramczyk, et al., Aberrant protein phosphorylation in cancer by using Raman biomarkers, Cancers 11 (2019) 2017.
[53] D. Fu, et al., Imaging the intracellular distribution of tyrosine kinase inhibitors in living cells with quantitative hyperspectral stimulated Raman scattering, Nat. Chem. 6 (2014) 614–622.
[54] M. Kopec, A. Imiela, H. Abramczyk, Monitoring glycosylation metabolism in brain and breast cancer by Raman imaging, Sci. Rep. 9 (2019) 166.
[55] Y. Liu, et al., Label-free molecular profiling for identification of biomarkers in carcinogenesis using multimodal multiphoton imaging, Quant. Imag. Med. Surg. 9 (2019) 742–756.
[56] X. Bi, B. Rexer, C.L. Arteaga, M. Guo, A. Mahadevan-Jansen, Evaluating HER2 amplification status and acquired drug resistance in breast cancer cells using Raman spectroscopy, J. Biomed. Optic. 19 (2014), 025001.
[57] M. Larion, et al., Detection of metabolic changes induced via drug treatments in live cancer cells and tissue using Raman imaging microscopy, Biosensors 9 (2019).
[58] A.T. Aron, A.G. Reeves, C.J. Chang, Activity-based sensing fluorescent probes for iron in biological systems, Curr. Opin. Chem. Biol. 43 (2018) 113–118.
[59] S. Fakih, et al., Monitoring intracellular labile iron pools: a novel fluorescent iron (III) sensor as a potential non-invasive diagnosis tool, J. Pharmacol. Sci. 98 (2009) 2212–2226.
[60] A.D. Sheftel, A.B. Mason, P. Ponka, The long history of iron in the Universe and in health and disease, Biochim. Biophys. Acta Gen. Subj. 1820 (2012) 161–187.
[61] D.B. Ott, A. Hartwig, M.J. Stillman, Competition between Al 3+ and Fe 3+ binding to human transferrin and toxicological implications: structural investigations using ultra-high resolution ESI MS and CD spectroscopy, Metall 11 (2019) 968–981.
[62] F.J. Alonso-García, E. Blanco-González, M. Montes-Bayón, An inductively coupled plasma-mass spectrometry (ICP-MS) linked immunoassay by means of iodinated antibodies for transferrin quantitative analysis in breast cancer cell lines, Talanta 194 (2019) 336–342.
[63] J.W. Pawlowski, N. Kellicker, C.E. Bobst, I.A. Kaltashov, Assessing the iron delivery efficacy of transferrin in clinical samples by native electrospray ionization mass spectrometry, Analyst 141 (2016) 853–861.
[64] S.M. Levchenko, Qu, J. Biomolecular component analysis of phospholipids composition in live HeLa cells, Biosensors 8 (2018).
[65] H. Najbjerg, et al., Monitoring cellular responses upon fatty acid exposure by Fourier transform infrared spectroscopy and Raman spectroscopy, Analyst 136 (2011) 1649–1658.
[66] I.W. Schie, et al., Direct comparison of fatty acid ratios in single cellular lipid droplets as determined by comparative Raman spectroscopy and gas chromatography, Analyst 138 (2013) 6662.